Fluidization behavior and reduction kinetics of pre-oxidized magnetite-based iron ore in a hydrogen-induced fluidized bed

Heng Zheng[1),✉], *Oday Daghagheleh*[1)], *Thomas Wolfinger*[2)], *Bernd Taferner*[1)], *Johannes Schenk*[1,2)], *and Runsheng Xu*[3)]

1) Chair of Ferrous Metallurgy, Montanuniversitaet Leoben, Franz-Josef-Straβe 18, 8700, Leoben, Austria
2) K1-MET GmbH, Stahlstraße 14, 4020 Linz, Austria
3) The State Key Laboratory of Advanced Metallurgy, University of Science and Technology Beijing, Beijing 100083, China

Abstract: The influence of different pre-oxidation temperatures and pre-oxidation degrees on the reduction and fluidization behaviors of magnetite-based iron ore was investigated in a hydrogen-induced fluidized bed. The raw magnetite-based iron ore was pre-oxidized at 800 and 1000°C for a certain time to reach a partly oxidation and deeply oxidation state. The structure and morphology of the reduced particles were analyzed via optical microscope and scanning electron microscopy (SEM). The reaction kinetic mechanism was determined based on the double-logarithm analysis. The results indicate that the materials with higher oxidation temperature and wider particle size range show better fluidization behaviors. The lower oxidation temperature is more beneficial for the reduction rate, especially in the later reduction stage. The pre-oxidation degree shows no obvious influence on the fluidization and reduction behaviors. Based on the kinetic analysis, the reduction progress can be divided into three stages. The reduction mechanism was discussed combing the surface morphology and phase structure.

Keywords: magnetite-based iron ore; prior oxidation; fluidization behavior; kinetic analysis; hydrogen reduction

1. Introduction

The European Union (EU) aims to reach the goal of climate neutrality (net-zero greenhouse gas emissions) by 2050 [1]. It is noticed that, nowadays, about 60% of the crude steel from Europe is produced through the blast furnace-basic oxygen furnace (BF-BOF) route [2]. The BF-BOF route has a high production efficiency but produces more CO_2 per ton of crude steel than other alternative steelmaking routes. Currently, steelmaking industry is still one of the major CO_2 emission sectors in Europe, which emits 4% of the EU's total CO_2 emissions [3]. The breakthrough technologies are required to further cut down CO_2 emissions [1,4–5]. Already, different alternative steelmaking processes have been investigated under the European Ultra Low CO_2 Steelmaking (ULCOS) program [4–5]. One of the interesting topics is using hydrogen as a reducing agent instead of CO [6–11]. Hence no CO_2 will be generated during the reduction of iron oxides. There are some promising related projects in the EU [12], such as HYBRIT in Sweden [13], SALCOS in Germany [14], and SuSteel and HYFOR® in Austria [15].

Direct reduction of iron ore fines receives increasing attention in ore-based ironmaking. The fluidized bed technology provides a possibility to produce direct reduced iron (DRI) with H_2 and iron ore fines [16]. A pre-heating system for the iron ore is required when using hydrogen as the reducing agent due to the endothermic reaction. It is also difficult to process all types of iron oxides in the form of iron ore fines. In the case of magnetite-based iron ore, the pre-heating can be done via a gas with a remaining amount of oxygen to utilize the exothermic oxidation reaction from Fe_3O_4 to Fe_2O_3. Based on our previous work [17–20], in an H_2-induced fluidized bed reactor, the magnetite-based iron ore showed the lowest reducibility and the worst fluidization behaviors due to the formation of a dense iron shell on the particle surface. Though, the same amount of the generated energy due to the oxidation is needed for the reduction afterwards, the pre-oxidation treatment improves the reduction efficiency and fluidization behaviors significantly. Some other researchers studied the influence of the pre-oxidation treatment using thermogravimetric analyzers. Based on the research from Wolfinger *et al.* [21], Park and Ostrovski [22], and Wang *et al.* [23], the reducibility was also greatly enhanced due to the structural transformation from dense to porous phase, and the diffusion was not the rate-limiting step due to the formation of micro-cracks.

However, the above studies mainly focused on the reduction and fluidization behavior under various reducing conditions. Little attention has been given to the pre-oxidation treatment process. Furthermore, the influences of different

Springer

1874

Int. J. Miner. Metall. Mater., Vol. 29, No. 10, Oct. 2022

pre-oxidation temperatures and pre-oxidation degree on the reducibility of magnetite-based iron ores are rarely discussed. The scope of this work is to study the effect of different pre-oxidation treatments, i.e., different pre-oxidation temperatures and pre-oxidation degrees, on the fluidization behaviors, morphology, and thus reduction kinetics using hydrogen as reducing agent. The structure and morphology of the reduced particles were analyzed via optical microscope and scanning electron microscopy (SEM). The reaction kinetic mechanism was determined based on the double-logarithm analysis. This work will provide preliminary guidance for the performance optimization in a possible novel industrial-scale direct reduction process.

2. Experimental

2.1. Preparation of the oxidized material

In this work, a low-grade magnetite-based iron ore was used as the raw material. The chemical composition was characterized by the inductively coupled plasma-mass spectrometry (ICP-MS) method and is listed in Table 1. The MgO powder (>99.5wt% MgO, size below 44 μm) with high purity was used as anti-sticking agent during the experiments. The raw material was divided into three particle size ranges: 125–250 μm, 250–500 μm, and full size. The full size was achieved by mixing 50wt% of 125–250 μm and 50wt% of 250–500 μm. It should be noted that the particle size was defined by conventional dry sieving. For a pre-oxidation treatment, 1000 g of the raw material was charged into a 250 mm × 350 mm steel vessel and put into a conventional heat treatment furnace at 800 and 1000°C for a defined oxid-

Table 1. Chemical composition of the sample   wt%

Sample	Fe_{tot}	FeO	SiO_2	Al_2O_3	CaO	MgO	MnO	P
Raw magnetite	59.50	19.66	7.05	1.13	3.03	2.00	0.17	0.70

Note: Fe_{tot}—Total iron content.

ation time to reach a so-called deeply oxidation and partly oxidation. The bed height of the material layer was around 2.5 mm, ensuring a uniform contact between gas and solid. Based on the previous study [20], the raw magnetite-based iron ore could not maintain completed fluidized at 700°C reducing conditions. A deeply oxidation treatment and an addition of 0.5wt% MgO powder improved the fluidization significantly. Therefore, 7 different pre-oxidized materials were prepared for further reduction tests in this study, as shown in Table 2. It should be noted that for the material with bigger particle size, it took 8 h to reach a partly oxidation at 800°C. The additional amount of MgO powder was chosen as 0.5wt% for all the pre-oxidized materials. The oxidation degree (w) was determined by the weight gain as given in Eq. (1) [24–25]. It was impossible to obtain the oxidized material with a fixed oxidation degree, even under the same oxidation conditions. The oxidation degrees of the deeply oxidized material (DOX) and partly oxidized material (POX) were in the ranges of 50%–65% and 94%–97%, respectively.

$$w = \frac{\Delta m}{\Delta m_{theory}} \times 100\% \tag{1}$$

where Δm and Δm_{theory} are the measured weight gain and the theoretical weight gain for complete oxidation, respectively. Δm_{theory} is calculated based on the FeO content from the chemical analysis of the magnetite-based iron ore.

Table 2. The pre-oxidation treatments and oxidation degrees of the pre-oxidized materials

No.	Oxidized material	Size range / μm	Pre-oxidation temperature / °C	Oxidation time / h	Oxidation degree / %
1	$DOX_{125-250}$-1000	125–250	1000	8	97.67
2	$DOX_{250-500}$-1000	250–500	1000	8	96.61
3	$DOX_{125-500}$-1000	125–500	1000	8	94.61
4	$POX_{125-250}$-800	125–250	800	4	54.93
5	$POX_{250-500}$-800	250–500	800	8	59.51
6	$POX_{125-500}$-800	125–500	800	8	58.91
7	$DOX_{125-250}$-800	125–250	800	8	96.14

2.2. Experimental procedure

The experimental apparatus, a fluidized bed reactor with a bed diameter of 68 mm [19] and the reduction test procedure [20], have been already described in detail in previous publications. The basic concept of the experimental apparatus was to maintain a constant temperature and measure the weight loss and pressure drops during the reduction process. The reduction degree (RD) was defined through Eqs. (2)–(4) [18–21].

$$RD = \left(1 - \frac{O_{\text{bounded to Fe at } t=t_i}}{O_{\text{bounded to Fe at } t=t_0}}\right) \times 100\% \tag{2}$$

$$O_{\text{bounded to Fe at } t=t_i} = \frac{O_{\text{bounded to Fe}_2\text{O}_3} + O_{\text{bounded to FeO}} - \Delta m}{M_O}, \text{ in mol} \tag{3}$$

$$O_{\text{bounded to Fe at } t=t_0} = 1.5 \times \frac{m_0 \times Fe_{tot}}{M_{Fe}}, \text{ in mol} \tag{4}$$

where $O_{\text{bounded to Fe at } t=t_0}$ and $O_{\text{bounded to Fe at } t=t_i}$ are the amount of O bonded to Fe at the start and during the reduction; Δm and m_0 are the weight loss due to the loss of O and the mass of input material; M_O and M_{Fe} are the constant molar masses for O and Fe; $O_{\text{bounded to Fe}_2\text{O}_3}$ and $O_{\text{bounded to FeO}}$ are the amount of O bonded to Fe_2O_3 and the amount of O bonded to FeO; t is the reduction time; t_0 and t_i are the times of reaction where it starts and is during the reduction.

The superficial gas velocity was kept constant at 0.4 m/s at 700°C reduction temperature. This was achieved by a constant H_2 flow rate of 15.9 L·min^{-1} and balanced by nitrogen with a flow rate of 8.5 L·min^{-1}. When the RD reached 95% or the reaction time reached 85 min, the reducing gas was replaced by N_2, and the sample was cooled under N_2 atmosphere to ambient conditions. The obtained reduced samples were sealed in a plastic sample bag for further analysis.

2.3. Determination of the de-fluidized index

Some researchers defined the sticking ratio based on the weight ratio of the agglomerates and the total bed material after reduction [26–28]. However, in this work, no agglomerates were observed. To quantitatively describe the fluidization behavior, a de-fluidized index (DFI) was defined, as shown in Eq. (5), based on the measured ($\Delta p_{measured-bed}$) and theoretical ($\Delta p_{calculated-bed}$) differential pressure drops over the material [20]. The measured pressure drop caused by the grid and the material portion (dot gray line) is shown in Fig. 1(a). The black line represents the theoretical differential pressure drop over the material, which can be calculated based on Eq.

(6) [18,20]. The red dashed line represents the differential pressure for only the material in the fluidized bed without the pressure drop of the grid. This line should equal the black line when the material is entirely fluidized. However, when the material was completely fluidized, there were still minor deviations between $\Delta p_{measured-bed}$ and $\Delta p_{calculated-bed}$. This can be explained by the entrained material and some inaccuracies while measuring the differential pressure across the grid during the reduction [18]. Fig. 1(b) shows the DFI and RD against the reduction time. When DFI is smaller than 5%, it can be considered as a completely fluidization state.

$$\text{DFI} = \frac{\Delta p_{calculated-bed} - \Delta p_{measured-bed}}{\Delta p_{calculated-bed} - \Delta p_{Fixed-bed}} \quad (5)$$

$$\Delta p_{calculated-bed} = \frac{m_t \cdot g}{\text{Reactor area}} \quad (6)$$

where $\Delta p_{Fixed-bed}$ is the differential pressure drop when the material is in a fixed bed state; $\Delta p_{Fixed-bed}$ is 2 mbar (200 Pa) in this work; m_t is the mass of the material in the fluidized bed during the reduction; g is acceleration of gravity, where the value is 9.8 N/kg.
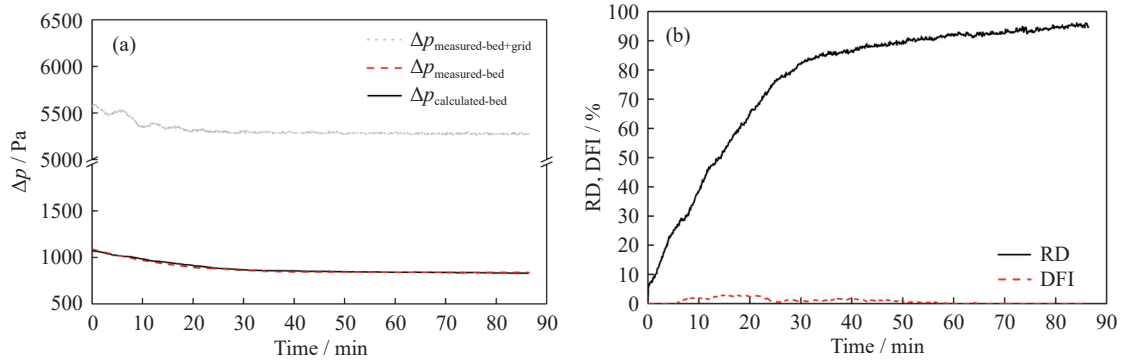

Fig. 1.   Fluidized reduction results for DOX$_{125-250}$-1000: (a) pressure drop against time; (b) RD and DFI against time.

2.4. Sample characterization

The morphology and internal structure of the samples were observed by scanning electron microscopy (Quanta 200Mk2, FEI, America) and optical light microscope (Nikon MM 40 measuring microscope system, Japan). The pore structures of the oxidized materials were evaluated by N_2 gas adsorption method using TriStar 3000 surface area analyzer (Micromeritics, America). The specific surface area was determined by Brunauer–Emmett–Teller (B.E.T.) method after degassing of the samples at 200°C for 2 h. The cumulative pore volume and average pore diameter were analyzed using Barrett–Joyner–Halenda (B.J.H.) method.

3. Results and discussion

3.1. BET-BJH analysis of pore structure

In this study, B.E.T. and B.J.H. methods were used to investigate the pore structures after the oxidation of the magnetite-based iron ore fines. Each test was repeated three times. The results of the pore structure parameters are listed in Table 3. The material oxidized at 1000°C is not shown due to the very low specific surface area (<0.01 m^2/g), which was beyond the valid range of the testing facility. The material with a smaller particle size presented slightly higher specific surface area and total pore volume. The specific surface area and the total pore volume of the raw magnetite were 0.092–

Table 3.   Pore structure parameters of the raw magnetite and oxidized samples

Sample	Particle size / μm	Specific surface area / (m^2·g^{-1})	Average pore size / nm	Total pore volume / (10^{-4} cm^3·g^{-1})
Raw magnetite	125–250	0.092 ± 0.001	10.887 ± 0.091	0.880 ± 0.014
	250–500	0.093 ± 0.003	10.467 ± 0.521	0.850 ± 0.085
POX-800	125–250	0.173 ± 0.002	5.160 ± 0.037	2.710 ± 0.057
	250–500	0.141 ± 0.006	5.120 ± 0.012	2.400 ± 0.078
DOX-800	125–250	0.025 ± 0.013	5.019 ± 0.261	0.350 ± 0.071

0.093 m^2/g and 0.850 × 10^{-4}–0.880 × 10^{-4} cm^3/g, respectively. The values of the specific surface area of POX$_{125-250}$-800 and POX$_{250-500}$-800 increased to 0.173 and 0.141 m^2/g. The values of the total pore volume increased to 2.710 × 10^{-4} and 2.400 × 10^{-4} cm^3/g, which were approximately three times larger than those of the raw magnetite. The specific surface area and total pore volume of DOX$_{125-250}$-800, however, decreased to 0.025 m^2/g and 0.350 × 10^{-4} cm^3/g. When the oxidation temperature increased to 1000°C, the specific surface area sharply reduced to less than 0.01 m^2/g. Theoretically, the crystal transformation from magnetite phase to hematite phase involves a volume expansion, but sintering effect would weaken the expansion trend and even contract the volume [29]. The average pore size of the raw magnetite was around 10 nm. After oxidation, the average pore size of all the materials decreased to around 5 nm. The average pore size gave a hint that microcracks occurred after the oxidation. The cracks generated many more pores with sizes around 5 nm.

Fig. 2 shows the surface morphology of the samples before and after oxidation. The raw magnetite showed a smooth surface with clear edges and corners. As shown in Fig. 2(f), the surface of the POX$_{125-250}$-800 sample was porous and covered by tiny whiskers. These whisker structures still showed clear edges, while, due to the sintering effect, as

shown in Fig. 2(g), the DOX$_{125-250}$-800 sample presented a smoother and denser surface. The sintering effect was more obvious for the oxidation temperature of 1000°C, as shown in Fig. 2(h).

3.2. Effect of pre-oxidation temperature

The effect of pre-oxidation temperature on the fluidization and reduction behavior was studied using DOX$_{125-250}$-1000 and DOX$_{125-250}$-800. As shown in Fig. 3(a), the RD curve of the DOX$_{125-250}$-800 was similar to that of DOX$_{125-250}$-1000 in the early reduction stage. However, when RD reached 80%, DOX$_{125-250}$-800 showed a higher reduction rate than DOX$_{125-250}$-1000. It should be noted that the DFI of DOX$_{125-250}$-800 was much higher than that of DOX$_{125-250}$-1000. A higher oxidation temperature showed a better fluidization behavior. From the point of fluidization behavior, a high-temperature oxidation treatment is suggested. The reduction efficiency is also an essential issue in DRI production. Fig. 3(b) shows the characteristic reduction time to reach a specific RD. It took 8.45 min to reach RD of 33% and another 20.26 min to reach RD of 80% for DOX$_{125-250}$-1000. DOX$_{125-250}$-800 required the similar time to reach RD of 33% (7.93 min) and 80% (18.06 min). But compared with DOX$_{125-250}$-1000, it took nearly only half time for DOX$_{125-250}$-800 to reach RD of 95%. The lower pre-oxidation temperat-
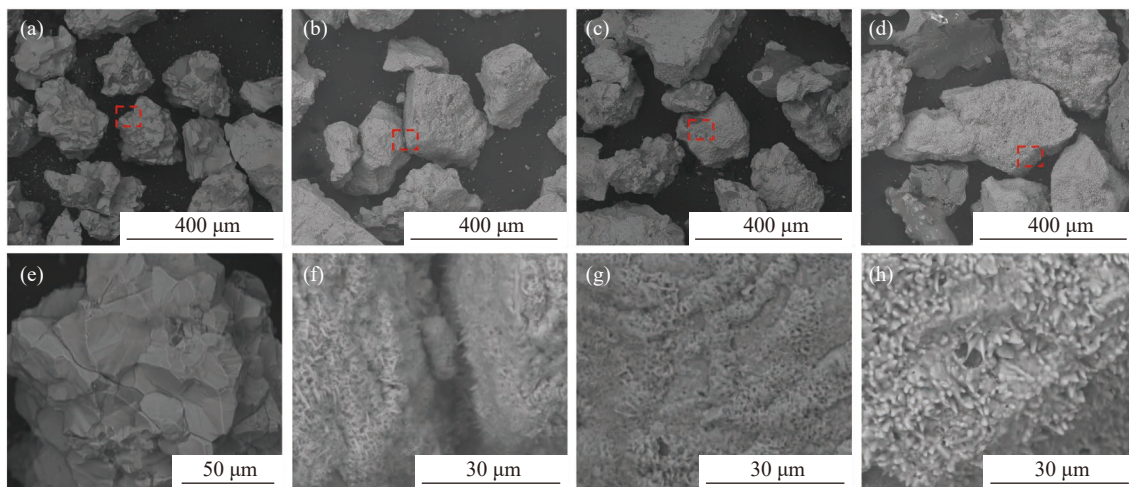

Fig. 2.   Samples with a particle size distribution of 125–250 μm: (a, e) raw magnetite; (b, f) POX$_{125-250}$-800; (c, g) DOX$_{125-250}$-800; (d, h) DOX$_{125-250}$-1000.
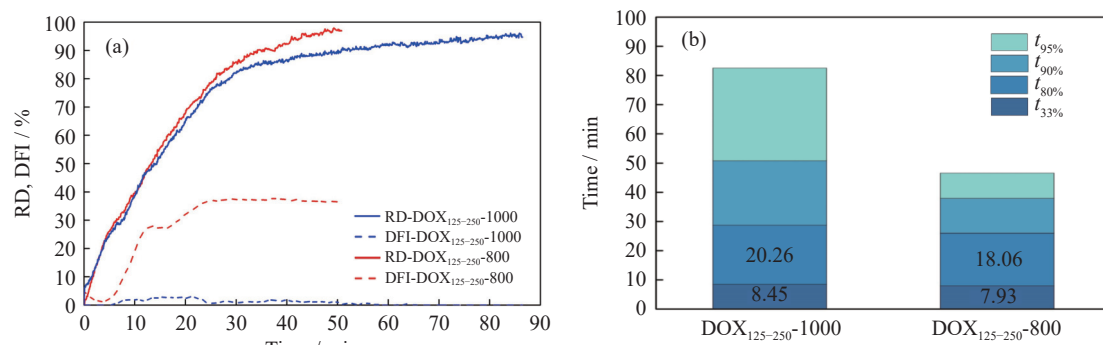

Fig. 3.   Effect of pre-oxidation temperature on the fluidization and reduction behaviors: (a) RD and DFI; (b) reduction time to reach a specific RD. $t_{33\%}$, $t_{80\%}$, $t_{90\%}$, and $t_{95\%}$ represent the required time for RD reaching 33%, 80%, 90%, and 95%, respectively.

ure is more beneficial for the reduction rate in the later reduction stage, which is explained from kinetic point of view in Section 3.5.

3.3. Effect of pre-oxidation degree

The effect of pre-oxidation degree on the fluidization and reduction behavior was studied using $DOX_{125-250}$-800 and $POX_{125-250}$-800. As shown in Fig. 4(a), the RD curve of the $DOX_{125-250}$-800 was similar to that of $POX_{125-250}$-800 in the entire reduction stage. However, the fluidization behaviors exhibited slightly different. The $POX_{125-250}$-800 started de-fluidization (DFI > 5%) when RD reached around 65%, while the $DOX_{125-250}$-800 started de-fluidization earlier at around RD of 35%. The two types of materials both showed a partly de-fluidized state in the end with a DFI of 36%. As for the characteristic reduction time, as shown in Fig. 4(b), there was no significant difference. Thus, the pre-oxidation degree shows no obvious difference in fluidization and reduction behaviors.

3.4. Effect of particle size

The effect of the particle size was investigated using the $POX_{125-250}$-800, $POX_{125-500}$-800, $POX_{250-500}$-800, $DOX_{125-250}$-1000, $DOX_{125-500}$-1000, $DOX_{250-500}$-1000. As shown in Fig. 5(a), $POX_{125-250}$-800 presented the highest reduction rate, which can be explained by the higher specific area and the better fluidization behavior of the material. The RDs of $POX_{125-500}$-800 and $POX_{250-500}$-800 exhibited similar trends before reaching 85%. It should be noted that the weight sig-

nal system is slightly influenced by the fluidization state of the materials in the fluidized bed. After reduction tests, the remaining materials were weighted again and compared to the final mass from the weight signal. The differences were within 1 g, which confirmed the mass balance and the accuracy of the data. Fig. 5(b) shows the DFI against RD of the partially oxidized material. $POX_{250-500}$-800 started partly de-fluidized at the beginning of the reduction process, indicating that the superficial gas velocity is not high enough for this particle size range. $POX_{125-250}$-800 and $POX_{125-500}$-800 started the de-fluidization when RD reached around 30% and 60%, respectively. In terms of the fluidization behavior, in this case, a wider particle size (125–500 μm) is more beneficial. The characteristic reduction times are listed in Table 4. For higher reduction efficiency, a small particle size (125–250 μm) is recommended.

Fig. 6 shows the effect of the particle size using $DOX_{125-250}$-1000, $DOX_{125-500}$-1000, and $DOX_{250-500}$-1000. As shown in Fig. 6(a), the $DOX_{125-250}$-1000 presented the highest reduction rate. The $DOX_{125-500}$-1000 exhibited a slightly higher reduction rate than $DOX_{250-500}$-1000, while the $DOX_{125-500}$-1000 and $DOX_{125-250}$-1000 showed much better fluidization behavior, as shown in Fig. 6(b), than $DOX_{250-500}$-1000. According to Table 4, it took 50.77 min for $DOX_{125-250}$-1000 to reach the RD of 90%, which was much less than those for the other two particle size range materials. $DOX_{250-500}$-1000 and $DOX_{125-500}$-1000 cannot reach the RD of 95% within the defined reduction time.
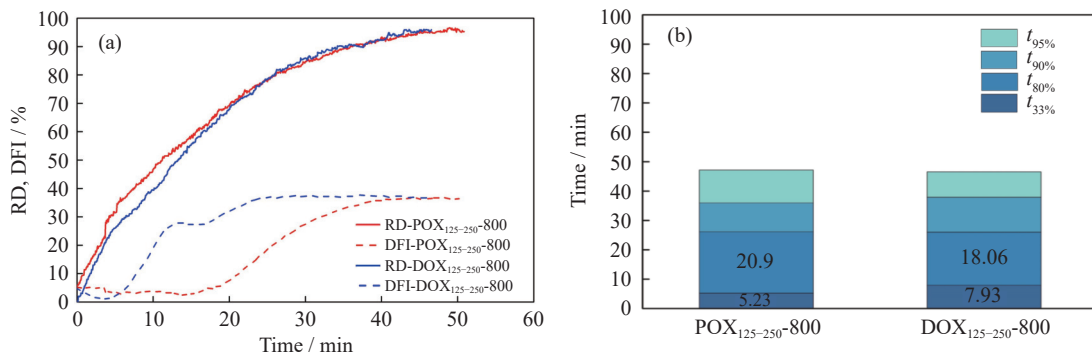

Fig. 4. Effect of pre-oxidation degree on the fluidization and reduction behaviors: (a) RD and DFI; (b) reduction time to reach a specific RD.
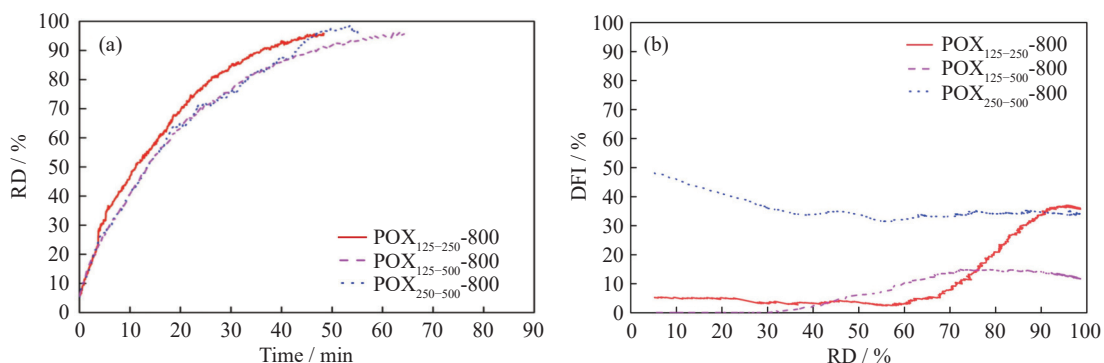

Fig. 5. Effect of particle size on the fluidization and reduction behaviors after pre-oxidized at 800°C: (a) RD; (b) DFI against RD.

Table 4.   The characteristic reduction times

Oxidized material	$t_{33\%}$ / min	$t_{80\%}$ / min	$t_{90\%}$ / min	$t_{95\%}$ / min
POX$_{125–250}$-800	5.23	26.13	35.96	47.16
POX$_{250–500}$-800	7.11	33.32	43.04	47.33
POX$_{125–500}$-800	7.20	32.54	46.95	60.01
DOX$_{125–250}$-1000	8.45	28.71	50.77	82.54
DOX$_{250–500}$-1000	8.94	37.07	74.48	—
DOX$_{125–500}$-1000	8.70	33.27	71.86	—

3.5. Analysis of the kinetic reaction mechanisms

3.5.1. Double-logarithm analysis method

The Avrami-Erofeev model is described as given in Eq. (7). Eq. (8) is obtained by taking double logarithm of both sides of Eq. (7). According to Hancock and Sharp [30], the value of n provides the information of the involved reaction mechanisms. Generally, if $n < 1$, the mechanism is considered as diffusion-controlled; if n is close to 1, the reaction is controlled by chemical reaction; if $n > 1.5$, the reaction is described by nucleation process [18,31–32].

$$1 - x = e^{-kt^n} \qquad (7)$$

$$\ln[-\ln(1-x)] = n\ln t + \ln k \qquad (8)$$

where x is the conversion (RD), n is the kinetic exponent, t is the reduction time (s), and k is rate constant. As shown in Fig. 7, the entire reduction process is divided into three stages: the

first stage ($0.11 < x < 0.33$), the second stage ($0.33 < x < 0.80$), and the third stage ($0.80 < x < 0.95$). An unavoidable fluctuation may occur when at the beginning of the reduction due to changing the atmosphere from inert to the reducing gas, which ends in a fluctuation of the system pressure. This kind of influence cannot be ignored due to the fast reduction in this stage. Therefore, the data from $x < 0.10$ was not taken into consideration. The n values are presented in Table 5.

For the first stage, the values of n were 0.76, 0.87, and 1.21 for DOX$_{125–250}$-1000, DOX$_{125–250}$-800, and POX$_{125–250}$-800, respectively. For the second stage, all the n values were close to 1, representing the chemical reaction control. For the third stage, the values of n were 0.49, 1.07, and 1.15 for DOX$_{125–250}$-1000, DOX$_{125–250}$-800, and POX$_{125–250}$-800, respectively. Therefore, the rate-limiting step was considered diffusion control in the early reduction stage for the deeply oxidized material. Higher pre-oxidation temperature (1000°C) influenced the final reduction stage, making the reaction controlled by diffusion, consistent with our previous result [20]. For partly oxidized material treated at 800°C, the whole reduction process was controlled by chemical reaction.

The double logarithm method considered the whole reaction process as three successive stages, each of which followed a single reaction model. The reduction of the iron oxide was regarded as several multiple reactions, where several reaction mechanisms may contribute to the same reaction
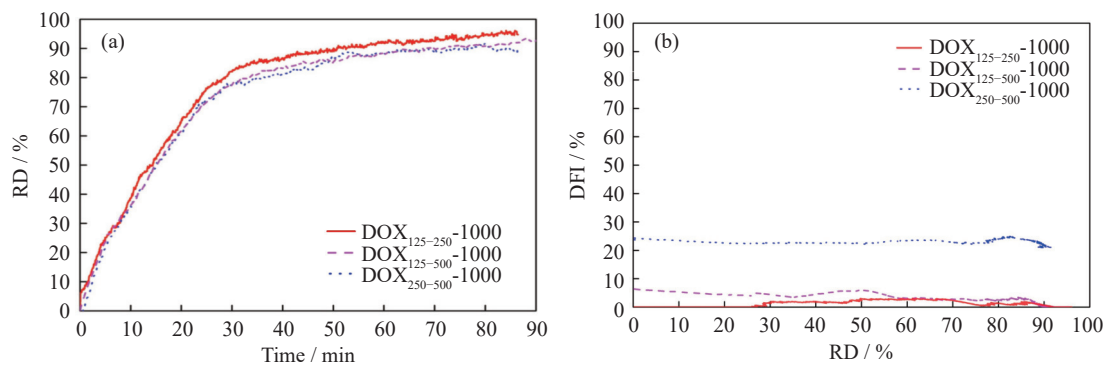
Fig. 6.   Effect of particle size on the fluidization and reduction behaviors after pre-oxidation at 1000°C: (a) RD; (b) DFI against RD.
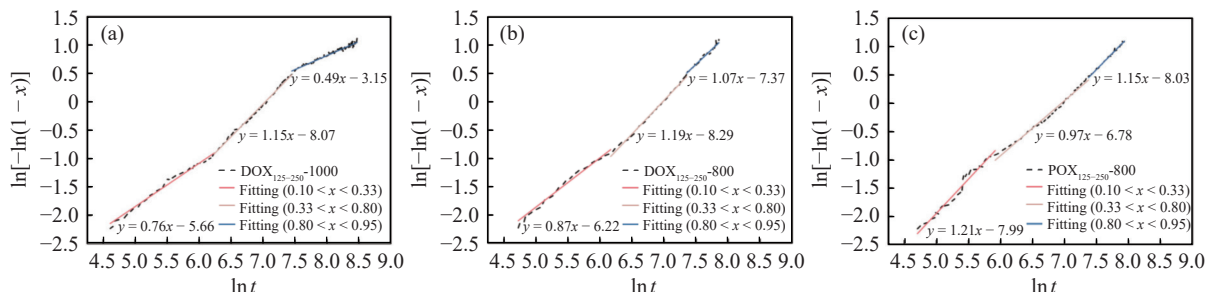
Fig. 7.   ln(−ln(1 − x)) vs. ln$t$ for different materials: (a) DOX$_{125–250}$-1000; (b) DOX$_{125–250}$-800; (c) POX$_{125–250}$-800.

Table 5.   The n values of the materials at different reduction stages

Reduction stage	DOX$_{125–250}$-1000	DOX$_{125–250}$-800	POX$_{125–250}$-800
First stage ($0.11 < x < 0.33$)	0.76	0.87	1.21
Second stage ($0.11 < x < 0.33$)	1.15	1.19	0.97
Third stage ($0.80 < x < 0.95$)	0.49	1.07	1.15

stage at the same time [18–19,31–36]. However, there is not a criterion for how to select a suitable method for the multiple reactions. Although the double-logarithm method cannot give information about the multiple reactions, this method shows the dominant reaction mechanism in each stage and is easier to be understood. To further confirm the kinetic reaction mechanism, the surface morphology and polished-section images of the samples should be examined.

3.5.2. Structural analysis

The surface morphology and the polished-section images of the reduced samples are shown in Fig. 8. The surfaces of the $DOX_{125-250}$-1000, $DOX_{125-250}$-800, and $POX_{125-250}$-800 presented a lamellar shape, a conical-shape, and a cylindrical shape, respectively. In Fig. 8(c), few conical-shaped irons can be observed, most of the iron phase exhibited cylindrical shapes. Nicolle and Rist [37] explained the growth of iron nucleus on wüstite and found a relationship between the shape of iron phase and the mechanism controlling step: when the reaction is restricted by the inward diffusion of iron ions, the newly formed iron phase shows a layer structure on the particle surface; when the reaction follows a chemical re-

action control, a cylindrical whisker may occur; if the reaction is under a mixed control by diffusion and chemical reaction, a conical shape of iron phase is supposed to be formed.

As discussed in Section 3.5.1, for $DOX_{125-250}$-1000, the reaction is controlled by diffusion, chemical reaction, and diffusion in the first, second, and third stage, respectively. The morphology shape in Fig. 8(a) is a typical shape for a diffusion-controlled reaction, which agrees the kinetic analysis for the third stage. As shown in Fig. 8(g), the polished-section image presents many wüstite islands due to the restriction of inward diffusion of iron ions. It can be concluded that the reduction of $DOX_{125-250}$-1000 is mainly controlled by the diffusion of iron ions. As for $DOX_{125-250}$-800 and $POX_{125-250}$-800, the morphology shapes in Fig. 8(b) and (c) are typical shapes for a mixed-controlled reaction and a chemical-controlled reaction, respectively. Based on the kinetic analysis, in the third stage, the diffusion is not the rate-limiting step for the reduction of $DOX_{125-250}$-800. Compared with $DOX_{125-250}$-1000, the wüstite islands in $DOX_{125-250}$-800 are less, as shown in Fig. 8(h). The whole reduction progress of $POX_{125-250}$-800 is only controlled by chemical reaction according to the kinetic ana-
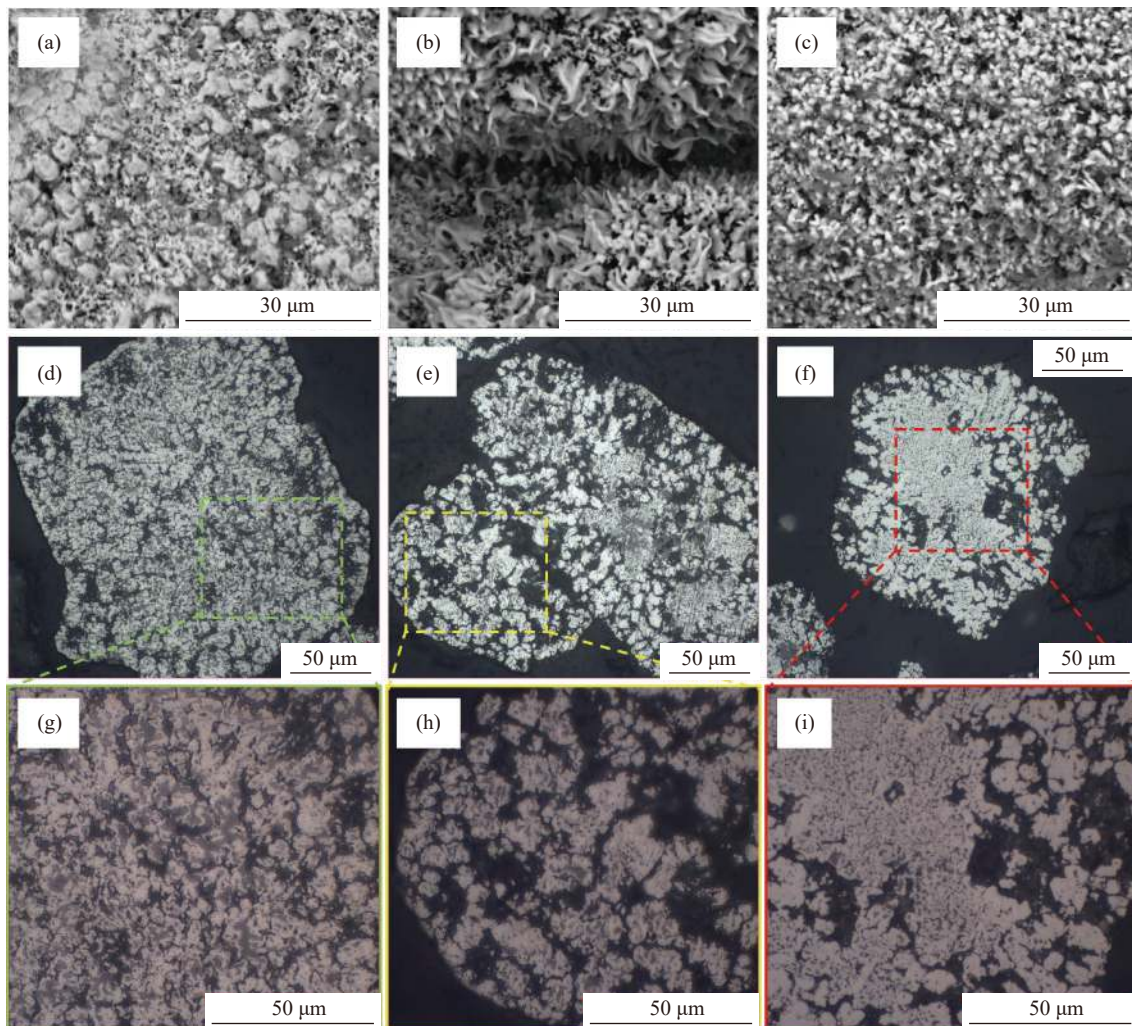

Fig. 8.   The reduced samples with the particle sizes of 125–250 μm: surface morphology of (a) $DOX_{125-250}$-1000, (b)$DOX_{125-250}$-800, and (c) $POX_{125-250}$-800; polished-section images of (d, g) $DOX_{125-250}$-1000, (e, h) $DOX_{125-250}$-800, and (f, i) $POX_{125-250}$-800. (a)–(c) were obtained by SEM; (d)–(i) were obtained by optical microscope.

1880

Int. J. Miner. Metall. Mater., Vol. 29, No. 10, Oct. 2022

lysis. Therefore, the diffusion of the iron ions is not a rate-limiting step. It is proved by the polished-section image, as shown in Fig. 8(i), the wüstite islands in $POX_{125-250}$-800 almost disappear.

Generally, the structure analysis supports the kinetic analysis. From the kinetic and structure analysis, it is found that a higher temperature pre-oxidation treatment results in a restriction of iron ion diffusion during the following reduction progress in the later stage. The surface morphology was flat and no whiskers were observed, which is beneficial to the fluidization behavior. A lower temperature pre-oxidation treatment helps to improve the diffusion of the iron ions. However, the surface morphology with whiskers destroys the fluidization behavior. In future work, more reduction conditions and pre-oxidation treatment parameters will be conducted to obtain a stable complete fluidization state.

4. Conclusions

The purpose of this work is to study the influence of the pre-oxidation temperature and pre-oxidation degree on the reduction and fluidization behaviors of the magnetite-based iron ore. Based on the current results, the following conclusions can be drawn:

(1) A partly oxidation of the magnetite-based iron ore with particle size of 125–500 μm at 800°C increased the specific surface area and total pore volume. Compared with the raw magnetite-based iron ore, the specific surface area and total pore volume for a deeply oxidation treatment at 800 and 1000°C decreased significantly.

(2) Under present experimental conditions, the materials with higher temperature pre-oxidation treatment showed better fluidization behaviors due to the flat surface morphology. The materials with lower temperature pre-oxidation treatment presented morphology with whiskers. From the point of fluidization behavior, a high-temperature oxidation treatment is suggested.

(3) Regarding on the reduction efficiency, a lower pre-oxidation temperature is more beneficial for the reduction rate, especially in the later reduction stage. The diffusion of the iron ions is improved. The pre-oxidation degree shows no noticeable difference in fluidization and reduction behaviors.

Acknowledgements

Conflict of Interest

All authors declare no financial/commercial conflicts of interest.

References

[1]   European Commission, *Climate Action - 2050 Long-term Strategy* [2021-11-13]. https://ec.europa.eu/clima/policies/strategies/2050_en

[2]   Worldsteel, *Steel Statistical Yearbooks* [2021-11-14]. https://www.worldsteel.org/steel-by-topic/statistics/steel-statistical-yearbook.html

[3]   Roland Berger, *The Future of Steelmaking–How the European Steel Industry can Achieve Carbon Neutrality*, Roland Berger GMBH, Munich, 2020.

[4]   European Commission, *Ultra-Low CO$_2$ Steelmaking* [2021-11-14]. https://cordis.europa.eu/project/id/515960

[5]   M.A. Quader, S. Ahmed, S.Z. Dawal, and Y. Nukman, Present needs, recent progress and future trends of energy-efficient Ultra-Low Carbon Dioxide (CO$_2$) Steelmaking (ULCOS) program, *Renewable Sustainable Energy Rev.*, 55(2016), p. 537.

[6]   A. Bhaskar, M. Assadi, and H.N. Somehsaraei, Decarbonization of the iron and steel industry with direct reduction of iron ore with green hydrogen, *Energies*, 13(2020), No. 3, art. No. 758.

[7]   Y.B. Chen and H.B. Zuo, Review of hydrogen-rich ironmaking technology in blast furnace, *Ironmaking Steelmaking*, 48(2021), No. 6, p. 749.

[8]   W.G. Liu, H.B. Zuo, J.S. Wang, Q.G. Xue, B.L. Ren, and F. Yang, The production and application of hydrogen in steel industry, *Int. J. Hydrogen Energy*, 46(2021), No. 17, p. 10548.

[9]   F. Patisson and O. Mirgaux, Hydrogen ironmaking: How it works, *Metals*, 10(2020), No. 7, art. No. 922.

[10] Primetals, *Enhanced Energy Efficient Steel Production – E³-SteP*, Primetals Technologies, 2019 [2021-11-14]. https://nachhaltigwirtschaften.at/resources/nw_pdf/events/20191009_highlights/spreitzer-rein-eisl_e3-step.pdf

[11] J. Tang, M.S. Chu, F. Li, C. Feng, Z.G. Liu, and Y.S. Zhou, Development and progress on hydrogen metallurgy, *Int. J. Miner. Metall. Mater.*, 27(2020), No. 6, p. 713.

[12] Bellona Europa, *Hydrogen in Steel Production: What is Happening in Europe – Part Two*, Bellona, 2021 [2021-11-14]. ht-

tps://bellona.org/news/industrial-pollution/2021-05-hydrogen-in-steel-production-what-is-happening-in-europe-part-two

[13] Hybrit, *Fossil-free Steel – A Joint Opportunity!* [2021-11-14]. https://www.hybritdevelopment.se/en/

[14] SALCOS®, *Our Program SALCOS* [2021-11-14]. https://salcos.salzgitter-ag.com/en/

[15] Voestalpine, *H2FUTURE* [2021-11-14]. https://www.voestalpine.com/greentecsteel/en/breakthrough-technologies/

[16] J.L. Schenk, Recent status of fluidized bed technologies for producing iron input materials for steelmaking, *Particuology*, 9(2011), No. 1, p. 14.

[17] S. Daniel, *Development of Characterization Methods for the Evalution of Kinetic Behavior and the Fluidization of Iron Ore Fines during Hydrogen-induced Fluidized Bed Reduction* [Dissertation], Montanuniversitaet Leoben, Leoben, 2000.

[18] D. Spreitzer and J. Schenk, Iron ore reduction by hydrogen using a laboratory scale fluidized bed reactor: Kinetic investigation—Experimental setup and method for determination, *Metall. Mater. Trans. B*, 50(2019), No. 5, p. 2471.

[19] D. Spreitzer and J. Schenk, Fluidization behavior and reducibility of iron ore fines during hydrogen-induced fluidized bed reduction, *Particuology*, 52(2020), p. 36.

[20] H. Zheng, D. Spreitzer, T. Wolfinger, J. Schenk, and R.S. Xu, Effect of prior oxidation on the reduction behavior of magnetite-based iron ore during hydrogen-induced fluidized bed reduction, *Metall. Mater. Trans. B*, 52(2021), No. 4, p. 1955.

[21] T. Wolfinger, D. Spreitzer, H. Zheng, and J. Schenk, Influence of a prior oxidation on the reduction behavior of magnetite iron ore ultra-fines using hydrogen, *Metall. Mater. Trans. B*, 53(2022), No. 1, p. 14.

[22] E. Park and O. Ostrovski, Reduction of titania-ferrous ore by hydrogen, *ISIJ Int.*, 44(2004), No. 6, p. 999.

[23] Z.Y. Wang, J.L. Zhang, K.X. Jiao, Z.J. Liu, and M. Barati, Effect of pre-oxidation on the kinetics of reduction of ironsand, *J. Alloys Compd.*, 729(2017), p. 874.

[24] D.Q. Zhu, C.C. Yang, J. Pan, and X.B. Li, Comparison of the oxidation behaviors of high FeO chromite and magnetite concentrates relevant to the induration of ferrous pellets, *Metall. Mater. Trans. B*, 47(2016), No. 5, p. 2919.

[25] F. Pan, Q.S. Zhu, Z. Du, and H.Y. Sun, Oxidation kinetics, structural changes and element migration during oxidation process of vanadium-titanium magnetite ore, *J. Iron Steel Res. Int.*, 23(2016), No. 11, p. 1160.

[26] Q.Y. Xu, Z.Z. Liu, Z.P. Li, J.J. Wang, and L. Zhou, The effect of carbon dissection of waste plastics on inhibiting the adhesion of fine iron ore particles during hydrogen reduction, *Metals*, 8(2018), No. 7, art. No. 523.

[27] Q.Y. Xu, Z.P. Li, Z.Z. Liu, J.J. Wang, and H.C. Wang, The effect of pressurized decarbonization of CO on inhibiting the adhesion of fine iron ore particles, *Metals*, 8(2018), No. 7, art. No. 525.

[28] M.I.A. Barustan and S.M. Jung, Morphology of iron and agglomeration behaviour during reduction of iron oxide fines, *Met. Mater. Int.*, 25(2019), No. 4, p. 1083.

[29] H. Zheng, J. Schenk, D. Spreitzer, T. Wolfinger, and O. Daghagheleh, Review on the oxidation behaviors and kinetics of magnetite in particle scale, *Steel Res. Int.*, 92(2021), No. 8, art. No. 2000687.

[30] J.D. Hancock and J.H. Sharp, Method of comparing solid-state kinetic data and its application to the decomposition of kaolinite, brucite, and $BaCO_3$, *J. Am. Ceram. Soc.*, 55(1972), No. 2, p. 74.

[31] E.R. Monazam, R.W. Breault, and R. Siriwardane, Reduction of hematite (Fe_2O_3) to wüstite (FeO) by carbon monoxide (CO) for chemical looping combustion, *Chem. Eng. J.*, 242(2014), p. 204.

[32] E.R. Monazam, R.W. Breault, R. Siriwardane, G. Richards, and S. Carpenter, Kinetics of the reduction of hematite (Fe_2O_3) by methane (CH_4) during chemical looping combustion: A global mechanism, *Chem. Eng. J.*, 232(2013), p. 478.

[33] H.S. Chen, Z. Zheng, Z.W. Chen, and X.T. Bi, Reduction of hematite (Fe_2O_3) to metallic iron (Fe) by CO in a micro fluidized bed reaction analyzer: A multistep kinetics study, *Powder Technol.*, 316(2017), p. 410.

[34] H.S. Chen, Z. Zheng, Z.W. Chen, W.Z. Yu, and J.R. Yue, Multistep reduction kinetics of fine iron ore with carbon monoxide in a micro fluidized bed reaction analyzer, *Metall. Mater. Trans. B*, 48(2017), No. 2, p. 841.

[35] K. He, Z. Zheng, Z.W. Chen, H.S. Chen, and W.P. Hao, Kinetics of hydrogen reduction of Brazilian hematite in a micro-fluidized bed, *Int. J. Hydrogen Energy*, 46(2021), No. 5, p. 4592.

[36] K. He, Z. Zheng, and Z.W. Chen, Multistep reduction kinetics of Fe_3O_4 to Fe with CO in a micro fluidized bed reaction analyzer, *Powder Technol.*, 360(2020), p. 1227.

[37] R. Nicolle and A. Rist, The mechanism of whisker growth in the reduction of wüstite, *Metall. Trans. B*, 10(1979), No. 3, p. 429.